Model of Organic Solar Cell Photocurrent Including the Effect of Charge Accumulation at Interfaces and Non-Uniform Carrier Generation

LORENZO TORTO[1] (Student Member, IEEE), ANDREA CESTER[1] (Senior Member, IEEE), ANTONIO RIZZO[1] (Student Member, IEEE), NICOLA WRACHIEN[1], SUREN A. GEVORGYAN[2], MICHAEL CORAZZA[2], AND FREDERIK C. KREBS[2]

1 University of Padua, 35131 Padua, Italy
2 Risø National Laboratory for Sustainable Energy, Technical University of Denmark, 4000 Roskilde, Denmark

CORRESPONDING AUTHOR: L. TORTO (e-mail: tortolor@dei.unipd.it)

ABSTRACT We developed an improved model to fit the photocurrent density versus voltage in organic solar cells. The model has been validated by fitting data from P3HT:PCBM solar cells. Our model quantitatively accounts for the band bending near the electrodes caused by charge accumulation in the active layer. The model explains the position of the built-in and the zero-field voltage, the value of the internal electric field, the impact of electrode materials, and the appearance of multiple inflections. In addition, the model can be used to monitor the cell condition during accelerated lifetests.

INDEX TERMS Organic solar cells, analytical model.

I. INTRODUCTION

Organic Solar Cells (OSCs) are a promising candidate for low-cost and sustainable power conversion from solar energy. The bulk heterojunction structure, based on the intimate contact between acceptor and donor species, permits an efficiency approaching 10% [1] and it is forecasted to reach 15% in the near future [2]. Their working principles are different from silicon solar cells, and there is interest in new measurement techniques and new models that provide new insights into the physical processes, which allow–and sometimes limit–the energy conversion. Among them, we may cite the exciton separation at the interface between the acceptor and donor [3] and the measurement of the built-in potential (V_{BI}), which defines the internal electric field and the upper boundary for the open circuit voltage [4].
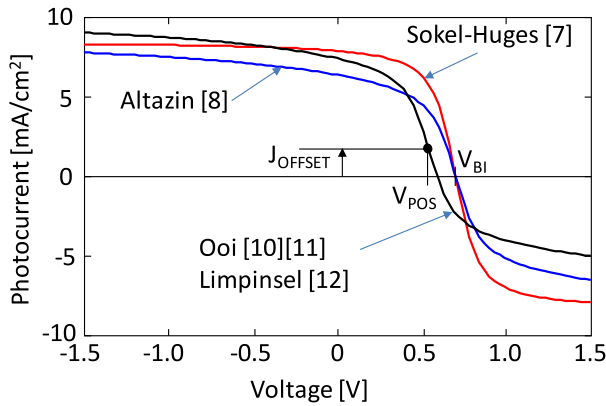
Some analytical models have already been proposed, although these are partially based on empirical or qualitative arguments [5], [6]. One of the first models used for OSC is the one introduced by Sokel and Hughes [7] to explain the photocurrent in insulators, assuming a constant electric field and a constant generation rate (G) within the active layer. The model predicts the photocurrent density-voltage (J_{PH}-V) relation shown in Table 1 and plotted in Fig. 1, which is an odd function with respect to the built-in potential V_{BI}. V_{BI} also represents the voltage at which J_{PH}=0, and it corresponds to the inflection point. Altazin *et al.* [8] improved this model including the Braun-Onsager polaron separation theory [3], [9], still assuming a constant electric field and a constant generation rate. However, the constant electric field leads to neglect the band bending at the interfaces between electrodes and active layers. Such bending produces a remarkable voltage drop which, in turn, may have a noticeable impact on photocurrent characteristics.

Further works [10]–[12] showed that the simple constant electric field approximation approach is not adequate for a correct estimate of the V_{BI} and the zero-photocurrent voltages. For instance, Ooi *et al.* [10] showed that if V=V_{BI}, there is still a non-zero current, deriving from carrier

TABLE 1. Model equations of some previous works.

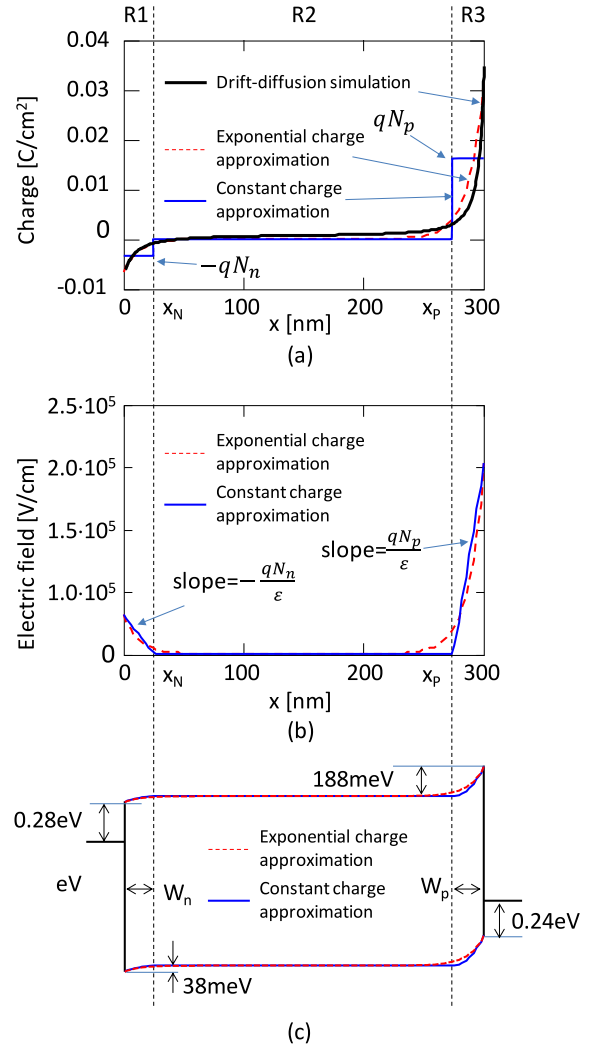| Model	Equation
Sokel [7]	$J_{PH} = qGL \left[coth\left(\frac{V - V_{BI}}{2V_T} \right) - \frac{2V_T}{V - V_{BI}} \right]$
Altazin [8]	$J_{PH} = P_{SEP} \cdot qGL \left[coth\left(\frac{V - V_{BI}}{2V_T} \right) - \frac{2V_T}{V - V_{BI}} \right]$
Limpinsel [12]	$J_{PH} = P_{SEP} qGL \left[coth\left(\frac{V - V_{POS}}{2V_T} \right) - \frac{2V_T}{V - V_{POS}} \right] + J_{OFFSET}$

FIGURE 1. Comparison between the Sokel-Hughes model [7]; The Limpinsel model [12]; Altazin model [8].

FIGURE 2. a) Simulation of the charge carrier accumulation. Solid blue lines represent the constant charge approximation at the interfaces, the red dotted curve is the exponential charge approximation, the bold black solid line is the charge profile predicted by a self-consistent drift diffusion simulation. The cathode is at x=0, and the anode is at x=L=300nm (in this case). b) electric field in the case of constant charge approximation (blue solid line) and exponential approximation (red dotted line). c) band diagram in the case of constant charge approximation (blue solid line) and exponential approximation (red dotted line). The values of the band bending are those obtained with the parameters values used to fit the curves in Fig. 3a. A comparison between band simulated by our model and drift diffusion model is shown in the inset of Fig. 8a.

diffusion due to the (partially) selective contacts, which may selectively block one of the two carriers. They also reported that multiple inflections may appear in the J_{PH}-V, ascribing them to the field dependence of the polaron separation rate, even though they gave only qualitative explanations.

Additional investigations of the shape of the J_{PH}-V were done by Limpinsel *et al.* [12]. They demonstrated that the point of symmetry (V_{POS} in Fig. 1) does not match V_{BI} and they included a constant current offset to the Sokel relation to account for the diffusion current observed by Ooi *et al.* [11] (J_{OFFSET} in Fig. 1), but they attributed this current to the band bending at the interfaces, which reduces the effective voltage across the blend. Consequently, the zero-electric field in the bulk of the blend – the so called quasi-flat-band condition– is expected at the voltage $V_{POS} < V_{BI}$. V_{POS} is still the point of symmetry of the J_{PH}-V introduced in the work of Ooi [11]. The comparison between Sokel and Limpinsel models is shown in Fig. 1, whereas the model equations are also reported in Table 1.

Still, although these models might allow for a simple first order approximation, they do not account for non-constant electric field and non-constant free carrier generation rate across the active layer.

In this work we propose an improved analytical model, which also takes into account the band bending at the

interfaces induced by the accumulated positive and negative polarons at the anode and cathode, respectively. In other words, unlike previous models, we considered the effects of non-constant electric field. We include in the model also a non-uniform carrier generation rate and the field dependent polaron separation probability. We validate the model correlating the theoretical and experimental results for fresh and aged devices. We highlighted the role of the band bending at the interfaces in the offset current, in the J_{PH}-V shape, and in the appearance of multiple inflection points in the J_{PH}-V.

II. MODEL DESCRIPTION

Our model is based on the following approximations:

1) Since the active layer is a blend of two organic materials, we consider the active layer as a single undoped material featuring the LUMO of the acceptor and the HOMO of the donor.

2) The difference between the Fermi levels in the active layer and the electrodes leads to an accumulation of negative polarons at the cathode interface and positive polarons at the anode interface. We verified by a drift diffusion numerical simulation that these charge distributions extend into the active layer for some tens of nanometers (see the black bold solid lines in Fig. 2a). These charge accumulations produce a voltage drop at the interfaces, which make the electric field not constant across the layer. In contrast to some previous models [7], [8], we analytically account for these voltage drops, and the non-constant electric field.

3) We consider that the charge distribution is independent on the applied bias, at least at reverse bias or moderate forward bias, i.e., when carrier injection is negligible.

4) Similarly, we approximate the charge distribution independent on the light condition. This approximation holds if the concentration of photogenerated carriers is small compared to the accumulated charge density at the interface.

5) We used a photogeneration G(x) exponentially decreasing within the active layer:

$$G(x) = G_0 e^{-\lambda x} \qquad (1)$$

where $\lambda > 0$ is the absorption coefficient. We assumed in all our simulations that the cell is illuminated from the cathode side (x=0). Since the absorption length of PCBM:P3HT blend depends on the incident light wavelength, we chose a value of 1/120nm. This value is close to the peak of the absorption length within the visible light reported in some works in [13] and [14]. Although this is still an approximation, this is a major improvement with respect to the previous works [7], [8], [10]–[12] which assumed, instead, a constant generation rate across the active layer.

6) Finally, we neglect the bimolecular recombination, in agreement with what was reported in [5] and [15]. In fact, we verified that in our cells there is a perfect linear dependence between the short circuit current and the incident light power. This is a signature of negligible bimolecular recombination as demonstrated in [5].

The real shape of the charge distribution must be found by using a drift diffusion simulation, which is complex and time consuming. For sake of simplicity, we adopted two possible shapes for the accumulated charge: 1) constant;

TABLE 2. Notations and constants used for our model.

Symbol	Meaning	Values assumed in our model
μ_n	Electron mobility	0.006 cm^{2}V^{-1}s^{-1}
μ_p	Hole mobility	0.01 cm^{2}V^{-1}s^{-1}
V_T	Thermal potential	25mV (at room temperature)
k	Boltzmann constant	1.38·10^{-23}JK^{-1}
T	Absolute temperature	300K
q	Elementary charge	1.6·10^{-19}C
a	Average molecular distance	1nm
ΔE	Exciton binding energy	$q/(4\pi\varepsilon a)$=0.48eV
ε	Dielectric permittivity	3 ε_0=2.65·10^{-13}F/cm
λ	Absorption coefficient	8.33·10^4 cm^{-1}
L	Active layer thickness	300nm or 315nm

2) exponential. Both are shown in Fig. 2a. The exponential distribution is close to the drift diffusion simulations, but the transport equations are more difficult to solve analytically. Instead, the constant charge distribution is easier to handle. Incidentally, the band bending predicted by the exponential charge distribution and constant charge distribution are very close to each other (see Fig. 2c).

In the following, we will focus on the constant charge accumulation at the interface, postponing the comparison of the constant and exponential distribution to Section IV.

The constant charge approximation allows to divide the cell into three regions (see Fig. 2):

R1) a negatively charged region at the cathode (x<W_n);
R2) a central quasi-neutral region (W_n<x<L-W_p);
R3) a positively charge region at the anode (x>L-W_p).

The charges in R1 and R3 generate an electric field (Fig. 2b) and, in turn, a voltage drop responsible for the band bending at the contacts (Fig. 2c). The electric field is linear, and the band bending is parabolic. In the quasi-neutral region R2 the electric field is constant.

The model is obtained starting from the continuity equations for electrons and holes:

$$-G(x) P_{SEP}(E) = \mu_n \frac{\partial E}{\partial x} n + \mu_n E \frac{\partial n}{\partial x} + V_T \mu_n \frac{\partial^2 n}{\partial x^2}$$

$$G(x) P_{SEP}(E) = \mu_p \frac{\partial E}{\partial x} p + \mu_p E \frac{\partial p}{\partial x} - V_T \mu_p \frac{\partial^2 p}{\partial x^2} \qquad (2)$$

where n and p are the photogenerated electron and hole concentrations inside the blend, respectively. See Table 2 for other constant values and notations. Noticeably, in contrast with previous analytical models approach [7], [8], we consider a spatially variable electric field (as in Fig. 2).

We account for the exciton separation probability (P_{SEP}) using the Braun-Onsager model [3]

$$P_{SEP}(E) = \frac{k_{SEP}(E)}{k_{SEP}(E) + k_{REC}} \qquad (3)$$

where k_{REC} is the polaron pair recombination rate and k_{SEP} is the polaron separation rate,

which is field dependent.

$$k_{SEP}(E) = k_{SEP0} \frac{J_1\left(2\sqrt{-2b}\right)}{2\sqrt{-2b}}$$

$$k_{SEP0} = \frac{<\mu> q}{\varepsilon} \frac{3}{4\pi a^3} e^{-\frac{\Delta E}{kT}}$$

$$b = \frac{q^3 |E|}{8\pi \varepsilon k^2 T^2} \tag{4}$$

where J_1 is the first order Bessel function, $<\mu>$ is the average carrier mobility, q is the elementary charge, $\varepsilon = 3\varepsilon_0$ is the dielectric permittivity of the active layer, a is the average molecular distance, ΔE is the exciton binding energy, k is the Boltzmann constant and T is the temperature. For further details on the Braun-Onsager model, the interested reader may refer to [3] and [9].

Noticeably, $k_{SEP}(|E|)$ follows a monotonically increasing behavior with a minimum in $E=0$ [3], and $k_{SEP}(0)=k_{SEP0}$, which is the separation rate when electricfield is zero.

At this point, it is worth to note that electric field is not constant across the active layer. In particular, $E(x)$ is constant inside the region R2, but it linearly increases in regions R1 and R3 (see Fig. 2b). Hence, the separation probability features a minimum in the bulk of the active layer (region R2) and it increases close to the electrodes (regions R1 and R3).

For sake of simplicity, we decide to assume $P_{SEP}(E)$ constant all over the active layer, and we use the P_{SEP} value calculated in R2. This approximation is reasonable because R2 represent the majority of the blend volume. Even though this might introduce a slight underestimate of the photocurrent, it strongly simplifies the analytical solution of the model equations, at least under the constant charge distribution approximation.

Solving (2) for $n(x)$ and $p(x)$ in each region, we write the electron and hole concentrations:

$$n(x) = \begin{cases} A_{R1}n1_{R1}(x) + B_{R1}n2_{R1}(x) + n0_{R1}(x) & R1 \\ A_{R2}n1_{R2}(x) + B_{R2}n2_{R2}(x) + n0_{R2}(x) & R2 \\ A_{R3}n1_{R3}(x) + B_{R3}n2_{R3}(x) + n0_{R3}(x) & R3 \end{cases}$$

$$p(x) = \begin{cases} C_{R1}p1_{R1}(x) + D_{R1}p2_{R1}(x) + p0_{R1}(x) & R1 \\ C_{R2}p1_{R2}(x) + D_{R2}p2_{R2}(x) + p0_{R2}(x) & R2 \\ C_{R3}p1_{R3}(x) + D_{R3}p2_{R3}(x) + p0_{R3}(x) & R3 \end{cases} \tag{5}$$

$n1_{Ri}$ and $n2_{Ri}$ are solutions of the homogeneous equations for electrons, $p1_{Ri}$ and $p2_{Ri}$ are solutions of the homogeneous equations for holes, and $n0_i$ and $p0_i$ are particular solutions in region Ri (where i=1,2,3) for electrons and holes respectively. For further details about the expression of the above-cited functions, the interested reader may refer to the Appendix.

A_{Ri}, B_{Ri}, C_{Ri}, and D_{Ri} are constants of integration determined using the proper boundary conditions:

- The electron and hole concentration continuity in the point x_N and x_P which separate region R1 from R2 and R2 from R3, respectively (see Fig. 2).
- The electron and hole current continuity in the points x_N and x_P.
- The zero carrier concentration at the electrodes, i.e., $n(0) = p(0) = 0$ at the cathode and $n(L) = p(L) = 0$ at the anode.

III. MODEL VALIDATION AND DISCUSSION

We validated the model by using P3HT:PCBM cells with an active layer of 315nm and area of 1 cm^2 fabricated at DTU (Roskilde, Dk). The cells were assembled in roll-to-roll compatible process with a mini-roll coater [16]. The front electrode (Flextrode) composed of an Ag grid, PEDOT:PSS and ZnO, and the back electrode consisting of PEDOT:PSS and an Ag grid enclose the blend of P3HT:PCBM.

Incidentally, for the correct photocurrent estimation we need to adjust the experimental data considering the parasitic series resistance (10Ω in this case), determined using impedance spectroscopy. Other works in literature found similar parasitic series resistance values [12]. The measurements were done by means of thermally controlled sample holder at the temperature T=300K. We illuminated the cell by using a white led illuminator. We calibrated the led intensity to reach a cell illumination level of 1Sun. Please see [17] and [18] for further details.

In Fig. 3a, our model excellently fits the experimental data in both fresh and degraded cells. The values of the fitting parameter are shown in Fig. 3b. In these cases the experimental data show the characteristics of photocurrent of P3HT:PCBM cells taken during constant current stress degradation at 70mA/cm^2 stressing current. The data has been taken from [17]. The interested reader may find further details about the experiment in [17].
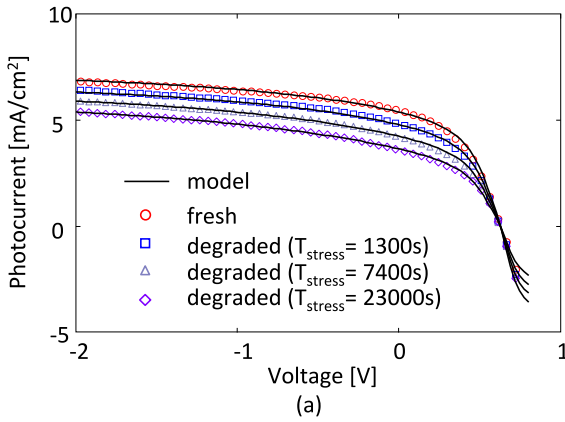
In this case, from our model, we can infer that the degradation changes only the generation rate G (which decreases from $4.2 \cdot 10^{21}$cm^{-3}s^{-1} to $3.45 \cdot 10^{21}$ cm^{-3}s^{-1}) and the recombination rate k_{REC}(which increases from $4 \cdot 10^3$s^{-1} to $8 \cdot 10^3$ s^{-1}). See Fig. 3b for the complete parameters set. G and k_{REC} affect the reverse-bias simulated photocurrent magnitude and the slope, respectively. A comparison with model of [12] shows that our model provides a better fit from 0V to 0.7V, thanks to the additional band bending introduced by the charge accumulation at the electrodes (Fig. 3c). Fig. 4a represents the simulated band bending in quasi-flat band condition, i.e., when the electric field is zero in the bulk of active layer. Fig. 4b shows the corresponding photogenerated electron and hole concentrations in quasi-flat band conditions. It is worth to remark that our model predicts asymmetrical electron and hole distributions with respect to the center of the active layer. This gives rise to the additional diffusion current J_{OFFSET}, still present in quasi-flat band condition, in agreement with what was only qualitatively predicted by Limpinsel *et al.* [12].

Incidentally, from Fig. 4b we calculate that photogenerated electron concentration is in the order of 10^{15}cm^{-3}at the cathode, i.e., one order of magnitude smaller than the fixed electron charge ($N_n=2 \cdot 10^{16}$cm^{-3} in this case).

Similarly, at the anode, the photogenerated hole concentration is two orders of magnitude smaller than the fixed charge ($N_p=10^{17}$cm^{-3} in this case).

In Fig. 5 we plot one output of our model (solid line), where we marked the following points:

1) The point of symmetry of the simulated photocurrent curve (V_{POS}), defined accordingly with [12];

2) The Built-In voltage V_{BI};

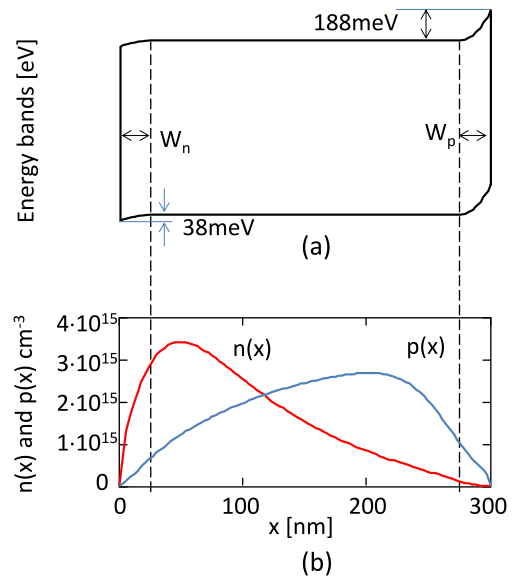3) V_{ZF} corresponding to the quasi-flat band condition, i.e., the voltage required to achieve zero-field in R2.

In the same plot, we also show a comparison with the behavior of the Limpinsel model (dotted line). Remarkably, in the model proposed by Limpinsel *et al.* [12] the quasi-flat band condition occurs at the same point of symmetry and J_{OFFSET} has been defined as the current flowing in quasi-flat band condition. For this reason, we plot in Fig. 5 the Limpinsel model using the same voltage as quasi-flat band condition (i.e., V_{ZF}). To obtain the dotted line in Fig. 5 we use $J_{OFFSET}=J_{PH}(V_{ZF})$ and we tuned the generation rate in order to achieve the best overlap between the two models in the region between -2V to 0.6V. Though the Limpinsel's first-order approximation is reasonable, it is not accurate when V>0.6V. In fact, Limpinsel model predicts that V_{POS} also identifies the quasi-flat band conditions. Following our model V_{POS} is different from V_{BI} (accordingly with [12]), but, even though V_{POS} is near V_{ZF}, it does not necessarily overlap to V_{ZF} in contrast with Limpinsel model (see Fig. 5, where $V_{ZF}<V_{POS}$). This implies that a correct evaluation of the operative voltages that characterize a solar cell cannot be done following that procedure, but needs a more accurate model.


Fitting parameter	Values			
	Fresh	T$_{STRESS}$=1300s	T$_{STRESS}$=7400s	T$_{STRESS}$=23000s
V_{BI}	0.78 V	0.78 V	0.78 V	0.78 V
$W_n=W_p$	25 nm	25 nm	25 nm	25 nm
N_n	2·10^{16}cm^{-3}	2·10^{16}cm^{-3}	2·10^{16}cm^{-3}	2·10^{16}cm^{-3}
N_p	10^{17}cm^{-3}	10^{17}cm^{-3}	10^{17}cm^{-3}	10^{17}cm^{-3}
G_0	4.2·10^{21}cm^{-3}s^{-1}	3.9·10^{21}cm^{-3}s^{-1}	3.7·10^{21}cm^{-3}s^{-1}	3.45·10^{21}cm^{-3}s^{-1}
k_{REC}	5·10^{3}s^{-1}	6·10^{3}s^{-1}	7.75·10^{3}s^{-1}	10·10^{3}s^{-1}
k_{SEP}	10^{4}s^{-1}	10^{4}s^{-1}	10^{4}s^{-1}	10^{4}s^{-1}
	Band bending derived from parameters above			
Cathode	38 meV	38 meV	38 meV	38 meV
Anode	188 meV	188 meV	188 meV	188 meV

(b)
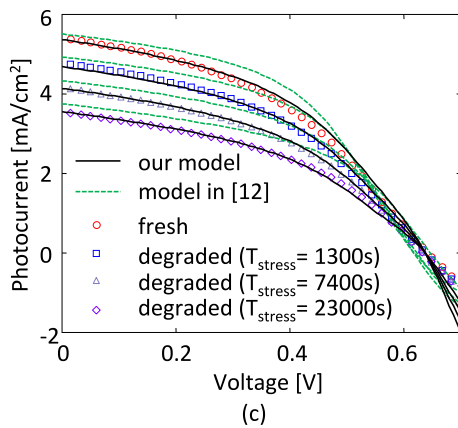
FIGURE 3. a) Comparison between experimental data and our model of fresh and stressed cells. **b)** Model parameter values used for fitting the experimental data in Fig. 3a. **c)** Comparison between our model and model in [12] in the range between 0V and 0.6V, highlighting the better fit of the proposed model thanks to the analytical approach accounting for the band bending at the interface.

FIGURE 4. a) Energy bands in quasi-flat band conditions where we highlight the value of the band bending at the interface. **b)** Concentrations of the photogenerated carriers in the same conditions of Fig. 3c.

Remarkably, it is possible to demonstrate that the carrier mobility values (μ_n and μ_p) do not affect the photocurrent shape simulated in Fig. 5, like in the model proposed by Sokel-Hughes. However, the electron and hole mobilities impact on the electron and holes concentrations, respectively: by increasing the mobility, the correspondent carrier concentration decreases. The mobility values can be obtained by the analysis of the J-V characteristics in dark [17] and/or other more sophisticated techniques, such as impedance spectroscopy [19].

TABLE 3. Expression of charge, electric field and potential for constant charge model and exponential charge model.

	CONSTANT CHARGE DISTRIBUTION MODEL		
	R1	R2	R3
Charge distribution Q(x)	$-qN_n$	0	qN_P
Electric field E(x)	$-\dfrac{qN_n}{\varepsilon}(x-x_N)+E_0$	E_0	$\dfrac{qN_p}{\varepsilon}(x-x_P)+E_0$
Potential V(x)	$+\dfrac{qN_n}{2\varepsilon}(x-x_N)^2-E_0x$	$-E_0x$	$-\dfrac{qN_p}{2\varepsilon}(x-x_P)^2-E_0x$

	EXPONENTIAL CHARGE DISTRIBUTION MODEL
Charge distribution Q(x)	$qN_p e^{\frac{x-L}{W_p}}-qN_n e^{-\frac{x}{W_n}}$
Electric field E(x)	$E_0+\dfrac{qN_pW_p}{\varepsilon}e^{\frac{x-L}{W_p}}+\dfrac{qN_nW_n}{\varepsilon}e^{-\frac{x}{W_n}}$
Potential V(x)	$-E_0x-\dfrac{qN_pW_p^2}{\varepsilon}e^{\frac{x-L}{W_p}}+\dfrac{qN_nW_n^2}{\varepsilon}e^{-\frac{x}{W_n}}$
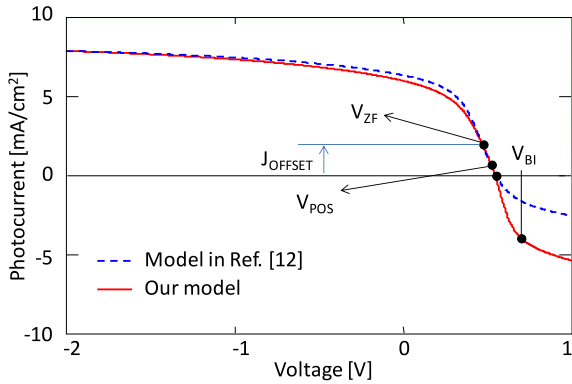
FIGURE 5. Output of our model (red solid line) compared to Limpinsel model (blue dotted line). In the plot we show the quasi-flat band condition voltage (V_{ZF}), the point of best symmetry (V_{POS}), the built-in potential (V_{BI}) and the $J_{OFFSET}=J_{PH}(V_{ZF})$ referred to our model.
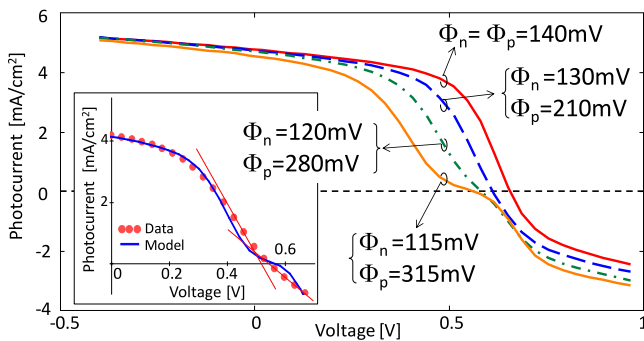
FIGURE 6. Effect of the barrier asymmetry on the appearance of inflections in photocurrent. Three inflections are detected when the barrier are appreciably asymmetric. The inset shows an example of fitting in a thermally stressed cell at 110°C for 4 hours when one interface is degrading allowing a larger barrier at the contact.
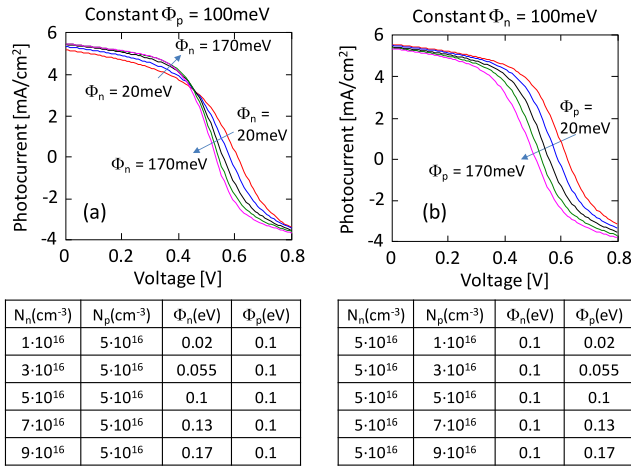
Finally, in [11] the appearance of three inflections in the photocurrent was related to the separation probability reduction, though in that work, the analysis was only qualitative. Our model can explain the multiple inflections by an asymmetric band bending at the two electrodes. In fact, referring to Fig. 2c the band bending at the cathode enhances the electron extraction due to the high electric field, but it acts as a small potential barrier against the hole extraction. The opposite occurs at the anode contact. If the barriers are almost symmetric only one inflection is detected. We were able to simulate the inflections in photocurrent imposing slightly different values in barrier heights. For instance, in Fig. 6 we show the fit of the photocurrent in a thermally degraded cell featuring three inflections, by increasing the cathode barrier height (see the inset of Fig. 6 for a comparison between experimental data and our model).

This model allows us also to assess the modifications, which may occur at the interface due to cell ageing and degradation in general. In fact, the model can detect any variation of the barrier heights, due to oxidation and other chemical reactions between, for instance, the contacts and contaminants either process-induced or those which may penetrate encapsulation during normal operations.

As an example, in Fig. 7 we plot two simulated photocurrents in which we assumed that a degradation occurred at the top interface (i.e., the illuminated side of the cell), shown in Fig. 7a, and at the bottom interface (i.e., the non-illuminated side of the cell), shown in Fig. 7b. Noticeably the two shapes are very different, and this is a signature of which interface had been degraded. In other words, one can take advantage of the model and perform a reliability assessment by means of only electrical measurement.

It is worth to remark that the proposed model simulates the active layer between two non-selective contacts, featuring an infinite extraction velocity. Clearly, a real solar cell may feature multiple interlayers between the active layers and the contacts, in order to improve the carrier extraction or to block selectively the carriers. The presence of such interlayers may be taken into account by imposing the suitable boundary

$N_n(cm^{-3})$	$N_p(cm^{-3})$	$\Phi_n(eV)$	$\Phi_p(eV)$
$1\cdot10^{16}$	$5\cdot10^{16}$	0.02	0.1
$3\cdot10^{16}$	$5\cdot10^{16}$	0.055	0.1
$5\cdot10^{16}$	$5\cdot10^{16}$	0.1	0.1
$7\cdot10^{16}$	$5\cdot10^{16}$	0.13	0.1
$9\cdot10^{16}$	$5\cdot10^{16}$	0.17	0.1

| $N_n(cm^{-3})$	$N_p(cm^{-3})$	$\Phi_n(eV)$	$\Phi_p(eV)$
$5\cdot10^{16}$	$1\cdot10^{16}$	0.1	0.02
$5\cdot10^{16}$	$3\cdot10^{16}$	0.1	0.055
$5\cdot10^{16}$	$5\cdot10^{16}$	0.1	0.1
$5\cdot10^{16}$	$7\cdot10^{16}$	0.1	0.13
$5\cdot10^{16}$	$9\cdot10^{16}$	0.1	0.17

FIGURE 7. Effect of the band bending variation on the photocurrent with: a) five different values of band bending Φ_n at the cathode and a constant Φ_p=0.1eV at the anode. b) five different values of band bending Φ_p at the anode and a constant Φ_n=0.1eV at the cathode. The tables below each plot show the value of charge concentrations N_n, N_p at the interfaces. The other fitting parameters are the same for all curves: W_n=W_p=25nm, V_{BI}=0.78V, G_0=4.82$\cdot10^{21}$cm^{-3}s^{-1}, k_{REC}=5$\cdot10^3$s^{-1}, k_{SEP}=10^4s^{-1}.

conditions, such as $J_n(0)$=0 for an ideal electrode blocking interlayer.

IV. COMPARISON BETWEEN EXPONENTIAL AND CONSTANT CHARGE MODELS

In Table 3 we show the comparison between the equations of charge distribution, electric field and potential for each model. Of course, the sharp distinction between the three regions disappears, even though we can still distinguish a negatively charged region near the cathode and a positively charged region near the anode, separated by a quasi-neutral region in the bulk of the active layer. Unlike the case of constant charge approximation, in the case of the exponential charge distribution, the equations cannot be analytically solved, but they need to be solved numerically.

Fig. 8a shows the comparison between the band diagrams in the case of constant charge distribution, exponential charge distribution and drift diffusion model. In this plot we used for the constant charge model the same parameters used to fit the fresh curve in Fig. 3a (red circles). For the exponential model, the fitting parameters have been tuned in order to keep constant the voltage drops and the total accumulated charge at the interfaces. In this case we used W_n=W_p=12.5nm, N_n=10^{16}cm^{-3}, N_p=5$\cdot10^{16}$cm^{-3}, and V_{BI}, G_0 k_{SEP}, k_{REC} are the same shown in Fig. 3b. Compared to the constant charge distribution, the exponential charge distribution allows for a much better approximation of the band diagram, which has been calculated using a much more time consuming drift diffusion simulation. The good match between the exponential model and the drift-diffusion simulation has been highlighted in the inset in Fig. 8a (red solid lines and black dotted line).
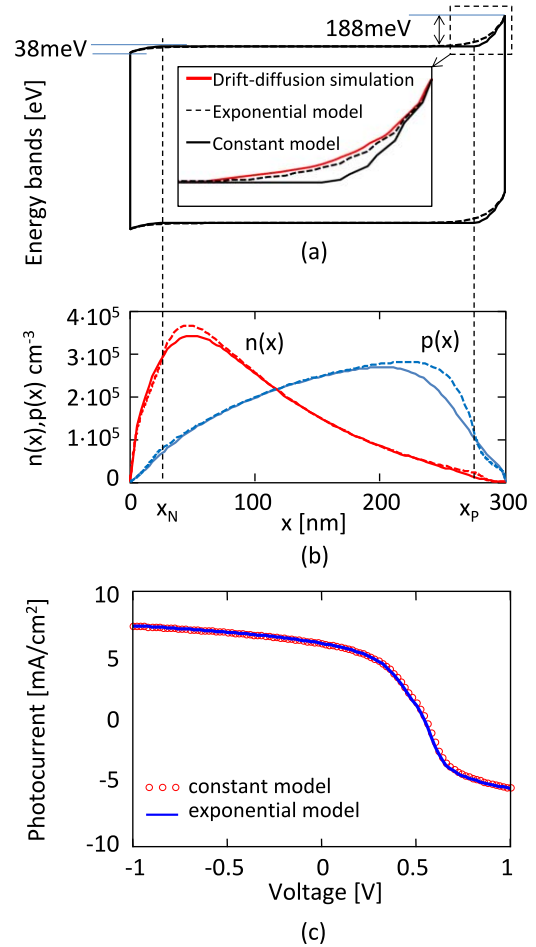
FIGURE 8. a) Comparison of the band diagram simulated with exponential (dotted line) and constant charge distribution (solid line) at the interfaces in quasi-flat band condition. The inset shows a zoom of the band bending at the anode and the comparison with the band shapes predicted with a drift diffusion simulation (red solid line). b) Photogenerated carrier distribution corresponding to the band diagram in Fig. 8a. Solid lines represent the constant charge model and dotted lines represent the exponential charge model. c) Comparison between the photocurrent simulated with the constant charge model (red circles) and exponential charge model (solid line).

At this point, some considerations are worth to be drawn. Even though the constant charge distribution does not allow a perfect band diagram estimate, a very good agreement exists between the predicted photogenerated carrier distributions, as shown in Fig. 8b. Moreover, the predicted photocurrents perfectly overlap each other, as shown in Fig. 8c. This suggests us that the photocurrent does not strongly depend on the particular shape of the charge distribution, but only on the measure of the band bending and on the magnitude of the electric field. Incidentally, these two quantities represent the selectivity and the carrier extraction capability of the contacts, respectively. In fact, a large band bending at the cathode, for example, acts as a barrier for holes, which attempt to exit from that electrode. On the other hand, the large electric field – consequence of the large band

TABLE 4. Notations and coefficients used in the homogeneous and particular solutions of equations (2).

Symbol	Value for electron continuity equation	Value for hole continuity equation
a_1	$-\dfrac{qN_n}{\varepsilon V_T}$	$\dfrac{qN_n}{\varepsilon V_T}$
a_2	$\dfrac{E_0}{V_T}$	$-\dfrac{E_0}{V_T}$
a_3	$\dfrac{qN_p}{\varepsilon V_T}$	$-\dfrac{qN_p}{\varepsilon V_T}$
x_1	$W_n + \dfrac{\varepsilon E_0}{qN_n}$	
x_3	$L - W_p - \dfrac{\varepsilon E_0}{qN_p}$	

bending – increases the electrons drift current, improving the carrier extraction. The opposite holds true at the anode.

This is the reason why we chose to focus our attention on the simple constant charge distribution model instead of the more complex exponential charge distribution model.

V. CONCLUSION

In this work we developed a model capable of quantitatively explain the shape of the J_{PH}-V, the position of the zero field voltage and the built-in potential. We quantitatively estimated the effect of the voltage drop at the electrodes and its effect on the internal electric field. Remarkably, we also found that the shape of the bending at the contact plays only a minor role in the J_{PH}-V shape. In addition, this model can be very helpful in calculating the electric field value inside the active layer, it can aid the interpretation of the appearance of multiple inflection points in the photocurrent and it can give indication about what interface is undergoing degradation during cell ageing.

Moreover, our model is an important tool for cells characterization and qualification and it can be also used during reliability assessment, monitoring the degradation of the cells by means of electrical noninvasive measurements.

APPENDIX

Electrons and holes concentrations $n(x)$ and $p(x)$ are expressed as a sum of the two homogeneous solutions and a particular solution of the differential equations (2), in each region. In region R1 and R3 the homogeneous solutions are:

$$n1_{R1}(x) = p1_{R1}(x) = e^{-\frac{a_1(x-x_1)^2}{2}}$$

$$n2_{R1}(x) = p2_{R1}(x) = \sqrt{-\frac{\pi}{2a_1}}e^{-\frac{a_1(x-x_1)^2}{2}}\,\mathrm{erf}\left(x\sqrt{-\frac{a_1}{2}}\right)$$

$$n1_{R3}(x) = p1_{R3}(x) = e^{-\frac{a_3(x-x_3)^2}{2}}$$

$$n2_{R3}(x) = p2_{R3}(x) = \sqrt{-\frac{\pi}{2a_3}}e^{-\frac{a_3(x-x_3)^2}{2}}\,\mathrm{erf}\left(x\sqrt{-\frac{a_3}{2}}\right) \quad (6)$$

where a_1 and a_3 are constants defined in Table 4 (second column for electrons and third column for holes), x_1 and x_3 are constants shown in Table 4 as well.

In region R2, where the electric field is constant, the homogeneous solutions become:

$$n1_{R2}(x) = p1_{R2}(x) = 1$$
$$n2_{R2}(x) = p2_{R2}(x) = e^{-a_2 x} \quad (7)$$

where a_2 is a constant defined in Table 4 as well.

The particular solutions in the three regions, are:

$$n0_{R1} = -\frac{G_0}{V_T\mu_n}\frac{1}{\lambda}\sqrt{-\frac{\pi}{2a_1}}e^{\frac{\lambda^2-a_1^2(x-x_1)^2}{2a_1}}\,\mathrm{erf}\left(\frac{\lambda-a_1(x-x_1)}{\sqrt{-2a_1}}\right)$$

$$p0_{R1} = -\frac{G_0}{V_T\mu_p}\frac{1}{\lambda}\sqrt{-\frac{\pi}{2a_1}}e^{\frac{\lambda^2-a_1^2(x-x_1)^2}{2a_1}}\,\mathrm{erf}\left(\frac{\lambda-a_1(x-x_1)}{\sqrt{-2a_1}}\right)$$

$$n0_{R2} = \frac{G_0}{V_T\mu_n}\frac{1}{\lambda^2-a_2\lambda}e^{-\lambda x}$$

$$p0_{R2} = \frac{G_0}{V_T\mu_n}\frac{1}{\lambda^2-a_2\lambda}e^{-\lambda x}$$

$$n0_{R3} = -\frac{G_0}{V_T\mu_n}\frac{1}{\lambda}\sqrt{-\frac{\pi}{2a_3}}e^{\frac{\lambda^2-a_3^2(x-x_3)^2}{2a_3}}\,\mathrm{erf}\left(\frac{\lambda-a_3(x-x_3)}{\sqrt{-2a_3}}\right)$$

$$p0_{R3} = -\frac{G_0}{V_T\mu_p}\frac{1}{\lambda}\sqrt{-\frac{\pi}{2a_3}}e^{\frac{\lambda^2-a_3^2(x-x_3)^2}{2a_3}}\,\mathrm{erf}\left(\frac{\lambda-a_3(x-x_3)}{\sqrt{-2a_3}}\right). \quad (8)$$

REFERENCES

[1] Q. Zhang *et al.*, "Small-molecule solar cells with efficiency over 9%," *Nat. Photon.*, vol. 9, pp. 35–41, Nov. 2015.

[2] M. C. Scharber and N. S. Sariciftci, "Efficiency of bulk-heterojunction organic solar cells," *Progress Polymer Sci.*, vol. 38, pp. 1929–1940, Dec. 2013.

[3] C. L. Braun, "Electric field assisted dissociation of charge transfer states as a mechanism of photocarrier production," *J. Chem. Phys.*, vol. 80, no. 9, pp. 4157–4161, 1984.

[4] M. Minghebach, C. Deibel, and V. Dyakonov, "Built-in potential and validity of the Mott–Schottky analysis in organic bulk heterojunction solar cells," *Phys. Rev. B*, vol. 84, Oct. 2011, Art. no. 153201.

[5] R. A. Marsh, C. R. McNeill, A. Abrusci, A. R. Campbell, and R. H. Friend, "A unified description of current–voltage characteristics in organic and hybrid photovoltaics under low light intensity," *Nano Lett.*, vol. 8, no. 5, pp. 1393–1398, 2008.

[6] B. Mazhari, "An improved solar cell circuit model for organic solar cells," *Solar Energy Mater. Solar Cells*, vol. 90, nos. 7–8, pp. 1021–1033, May 2006.

[7] R. Sokel and R. C. Hughes, "Numerical analysis of transient photoconductivity in insulators," *J. Appl. Phys.*, vol. 53, no. 11, p. 7414, Nov. 1982.

[8] S. Altazin *et al.*, "Analytical modeling of organic solar cells and photodiodes," *Appl. Phys. Lett.*, vol. 99, no. 14, p. 143301, Oct. 2011.

[9] L. Onsager, "Initial recombination of ions," *Phys. Rev.*, vol. 54, no. 8, pp. 554–557, Oct. 1938.

[10] Z. E. Ooi *et al.*, "On the pseudo-symmetric current–voltage response of bulk heterojunction solar cells," *J. Mater. Chem.*, vol. 18, pp. 1644–1651, Feb. 2008.

[11] Z. E. Ooi, T. L. Tam, A. Sellinger, and J. C. deMello, "Field-dependent carrier generation in bulk heterojunction solar cells," *Energy Environ. Sci.*, vol. 1, pp. 300–309, May 2008.

[12] M. Limpinsel, A. Wagenpfahl, M. Mingebach, C. Deibel, and V. Dyakonov, "Photocurrent in bulk heterojunction solar cells," *Phys. Rev. B*, vol. 81, no. 8, Feb. 2010, Art. no. 085203.

[13] Y. Kim *et al.*, "A strong regioregularity effect in self-organizing conjugated polymer films and high-efficiency polythiophene: Fullerene solar cells," *Nat. Mater.*, vol. 5, pp. 197–203, Mar. 2006.

[14] W. H. Lee, S. Y. Chuang, H. L. Chen, W. F. Su, and C. H. Lin, "Exploiting optical properties of P3HT: PCBM films for organic solar cells with semitransparent anode," *Thin Solid Films*, vol. 518, no. 24, pp. 7450–7454, May 2010.

[15] L. Liu and G. Li, "Investigation of recombination loss in organic solar cells by simulating intensity-dependent current–voltage measurements," *Solar Energy Mater. Solar Cells*, vol. 95, no. 9, pp. 2557–2563, 2011.

[16] J. E. Carlé *et al.*, "A laboratory scale approach to polymer solar cells using one coating/printing machine, flexible substrates, no ITO, no vacuum and no spincoating," *Solar Energy Mater. Solar Cells*, vol. 108, pp. 126–128, Jan. 2013.

[17] A. Rizzo *et al.*, "Effects of current stress and thermal storage on polymeric heterojunction P3HT:PCBM solar cell," in *Proc. IEEE Int. Rel. Phys. Symp. (IRPS)*, Pasadena, CA, USA, Apr. 2016, pp. 3C-2-1–3C-2-6.

[18] A. Cester *et al.*, "Effects of constant voltage and constant current stress in PCBM:P3HT solar cells," *Microelectron. Rel.*, vol. 55, nos. 9–10, pp. 1795–1799, 2015.

[19] A. Rizzo *et al.*, "Characterization and modeling of organic (P3HT:PCBM) solar cells as a function of bias and illumination," *Solar Energy Mater. Solar Cells*, vol. 157, pp. 337–345, Dec. 2016.

NICOLA WRACHIEN was born in Treviso, Italy, in 1982. He received the degree (*magna cum laude*) in electronic engineering and the Ph.D. degree in information engineering from the University of Padua, Italy, in 2006 and 2010, respectively, with a focus on advanced nonvolatile memories. He is currently a Post-Doctoral Fellow, researching on organic semiconductor devices.
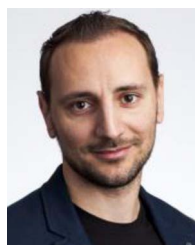
SUREN A. GEVORGYAN received the Ph.D. degree from the Technical University of Denmark, in 2010, where he is a Senior Scientist. He has been researching on organic photovoltaics and specializing in characterization and stability of the technology. His research interests involve new generation thin film PVs, device engineering, durability, and standard testing.

LORENZO TORTO (S'16) received the bachelor's degree in information engineering and the M.S. degree in electronic engineering from the Department of Information Engineering, University of Padua, in 2013 and 2016, respectively. His interests are in characterization, reliability, and modeling of polymeric solar cells.

MICHAEL CORAZZA received the master's degree in electronic engineering from the University of Padua, in 2013. He is currently pursuing the Ph.D. degree with the Technical University of Denmark. He has been working with photovoltaics since 2012, first with inorganic and then with organic PVs. His research interests involve degradation of devices and their advanced characterization (electron microscopes and mechanical tests).

ANDREA CESTER (M'98–SM'13) is an Associate Professor with the Department of Information Engineering, University of Padua, Italy. He has authored/co-authored over 180 papers published in international journals and conference proceedings. His research activities ranges: the characterization, reliability study, and modeling of organic electronic devices, photovoltaic devices, and RF-MEMS switches for reconfigurable antenna arrays.

ANTONIO RIZZO (S'15) was born in Legnago, Italy, in 1990. He received the M.S. degree in electronic engineering from the University of Padua, Padua, Italy, in 2014, where he is currently pursuing the Ph.D. degree in organic electronics, with a focus on organic photovoltaic devices.

FREDERIK C. KREBS received the Ph.D. degree from Technical University in 2000. Since 2000, he has been working on polymer solar cells and was appointed as a Full Professor in 2010. His research interests are printed solar cells with low environmental impact and the interplay between different disciplines that enable use of polymer solar cells in the energy system.